Nanoscale

Remarkable Long-Term Stability of Nanoconfined Metal-Halide Perovskite Crystals against Degradation and Polymorph Transitions

Journal:	*Nanoscale*
Manuscript ID	NR-ART-02-2018-001352.R1
Article Type:	Paper
Date Submitted by the Author:	30-Mar-2018
Complete List of Authors:	Kong, Xiaoqing; Stevens Institute of Technology, Department of Chemical Engineering and Materials Science Shayan, Kamran; Stevens Institute of Technology, Department of Physics Lee, Sangchul; Stevens Institute of Technology, Department of Chemical Engineering and Materials Science Ribeiro, Christian; Stevens Institute of Technology, Department of Chemical Engineering and Materials Science Strauf, Stefan; Stevens Institute of Technology, Department of Physics Lee, Stephanie; Stevens Institute of Technology, Department of Chemical Engineering and Materials Science

Nanoscale

ARTICLE

Received 00th January 20xx,
Accepted 00th January 20xx

DOI: 10.1039/x0xx00000x

www.rsc.org/

Remarkable Long-Term Stability of Nanoconfined Metal-Halide Perovskite Crystals against Degradation and Polymorph Transitions

Xiaoqing Kong,[a] Kamran Shayan,[b] Sangchul Lee,[a] Christian Ribeiro,[a] Stefan Strauf,[b] and Stephanie S. Lee *[a]

Metal-halide perovskites are promising candidates to advance optoelectronic devices but are known to suffer from rapid material degradation. Here we demonstrate that nanoconfinement is an effective strategy for the long-term stabilization of metal-halide perovskite $MAPbI_3$ crystals against humidity-induced degradation and temperature-induced polymorph transitions. Two-dimensional X-ray diffraction patterns of $MAPbI_3$ films reveal an unprecedented air-stability of up to 594 days in non-chemically modified, non-passivated $MAPbI_3$ films deposited on substrates imposing complete 2D confinement on the tens of nanometers length scale. Temperature-dependent x-ray diffraction analysis and optical spectroscopy further reveal the suppression of temperature-dependent phase transitions in nanoconfined $MAPbI_3$ crystals. Most notably, the high-temperature cubic phase of $MAPbI_3$, typically stable at temperatures above 327 K, remains present until a temperature of 170 K when the perovskite crystals are nanoconfined within the 100-nm diameter pores of anodized aluminum oxide templates. Photoluminescence mapping confirms that nanoconfined $MAPbI_3$ crystals exhibit spatial uniformity on the tens of microns length scale, suggesting that nanoconfinement is an effective strategy for the formation of high-quality, stable $MAPbI_3$ crystals across large areas.

Introduction

Over the past decade, metal-halide perovskite solar cells (PSCs) have emerged as frontrunners in the field of solution-processable solar cells due to their high power conversion efficiencies,[1–10] currently double that of leading organic solar cells,[11] and tunable optical and electronic properties based on their chemical composition. In particular, methylammonium lead iodide ($CH_3NH_3PbI_3$, denoted as $MAPbI_3$) has been extensively studied due to its superior optical and electronic properties. With a direct bandgap of 1.55 eV, corresponding to an absorption onset of 800 nm,[12] $MAPbI_3$ absorbs broadly across the visible solar spectrum. $MAPbI_3$ also exhibits high carrier mobilities,[13,14] ranging from 7.5 $cm^2\ V^{-1}\ s^{-1}$ for electrons to 12.5 – 66 $cm^2\ V^{-1}\ s^{-1}$ for holes.[15,16] These carriers recombine on a timescale of hundreds of nanoseconds, compared to a few nanoseconds in organic systems,[17] resulting in long diffusion lengths ranging between 100 – 1000 nm.[18,19]

Despite major improvements in device efficiency over the last few years, the stability of PSCs in humid environments, where also ultraviolet and thermal stresses are typically encountered, remains a significant challenge.[20,21] Exposure to humidity results in the formation of intermediate hydrated phases, leading to the reformation of PbI_2 and methylammonium iodide (MAI) after sufficient water has permeated the film.[22] When exposed to 55% humidity and 100-sun light intensity, $MAPbI_3$ was found to degrade into PbI_2 after 60 min due to the loss of MAI.[23] In a separate study, PSCs stored in ambient air retained less than 20% of their initial performance after 24 hours and only 5% after 6 days.[24] Many efforts have thus focused on improving the stability of PSCs using methods, such as chemical doping[25,26] and encapsulation,[27–29] with varying degrees of success. However, degradation still remains a key issue facing the commercialization of these devices.

In addition to humidity-induced degradation, $MAPbI_3$ also undergoes multiple polymorph transitions, one of which occurs within the operating temperature range of solar cells. At room temperature (RT), $MAPbI_3$ exists in a tetragonal phase (TP). At 327 K, a polymorph transition to the cubic phase (CP) occurs via rotation of Pb-I bonds.[30] A second low-temperature phase transition from TP to the orthorhombic phase (OP) exists in the range of 140 – 170 K,[31–33] depending on the processing details[32] and film morphology.[34] A number of studies have investigated differences between the optical,[31,35,36] thermal,[37] dielectric,[38] and photovoltaic[39] properties of the different phases. Neutron powder diffraction data revealed that the motion of MA cations in the OP of $MAPbI_3$ is restricted, while MA cations in the TP and CP can rotate at high frequency.[40,41] Electronically, the band gap of $MAPbI_3$ increases with decreasing lattice symmetry,[42] with the band gaps of the cubic, tetragonal and orthorhombic phases of $MAPbI_3$ calculated to be 1.3, 1.43 and 1.57 eV, respectively.[43] Accelerated recombination was observed in the

---

[a] *Department of Chemical Engineering and Materials Science, Stevens Institute of Technology, Hoboken, NJ 07030, USA.*

[b] *Department of Physics, Stevens Institute of Technology, Hoboken, NJ 07030, USA*

†Electronic Supplementary Information (ESI) available: [details of any supplementary information available should be included here]. See DOI: 10.1039/x0xx00000x

OP due to the small inclusions of TP, which act as charge recombination centers and may be detrimental for photovoltaic performance.[40] As a result of these factors, a significant power conversion efficiency decrease is observed near the tetragonal-orthorhombic transition.

A promising strategy to stabilize metastable polymorphs and influence crystallization outcomes is to nanoconfine crystals on the tens to hundreds of nanometers length scale. Previous work on organic small-molecule systems has demonstrated that nanoconfinement can significantly influence polymorph stability. Metastable β-glycine, for example, is stabilized in the nanopores of anodized aluminum oxide.[44] Another small molecule, glutaric acid, exhibits two polymorphs, α and β. When embedded in the nanometer-scale pores of controlled porous glass beads, metastable α-phase nanocrystals were stable for months at RT with no measurable transformation to the β-phase, the preferred polymorph in bulk crystals.[45] Such polymorph stabilization under nanoconfinement has also been observed in acetaminophen,[46–48] anthranilic acid,[49] and pimelic acid[45] crystals, and new polymorphs of pimelic acid, suberic acid, and coumarin were also discovered in nanopores.[45]

In the past two years, the incorporation of nanoporous scaffolds to confine perovskite crystallization in device platforms has been successfully demonstrated for both solar cells[50] and photodetectors.[51–53] As a viable strategy for perovskite-based device architecture, understanding the role of nanoconfinement on the crystal evolution of perovskites is critical for the further advancement of these technologies. We recently observed the stabilization of metastable PbI_2:DMF complexes in the nanopores of AAO templates.[54] When deposited in these templates, 2D x-ray diffraction imaging revealed that PbI_2:DMF crystals preferentially orient along the long axis of the pores, such that alternating sheets of PbI_2 and DMF molecules lie parallel to the long pore axis. Nanoconfined $MAPbI_3$ crystals in AAO templates were found to be stable in air for a period of two weeks, the same time period in which unconfined crystals completely degraded into PbI_2. Here we demonstrate both air stability up to 594 days, the longest observed thus far for undoped and non-passivated $MAPbI_3$ films, and suppression of polymorph phase transitions by utilizing nanoconfinement as a strategy to prevent degradation in solar cell applications.

Results and discussion

To determine the effect of nanoconfinement on $MAPbI_3$ crystallization, polymorphism, and stability, we formed $MAPbI_3$ films on substrates with varying extents of confinement. Specifically, MAI and PbI_2 precursors were spin coated from co-solutions onto flat SiO_2/Si substrates with a) no confinement, b) vertically oriented AAO nanorods with lengths and diameters of ~300 – 400 nm and 30 nm, respectively, that imposed partial confinement in two-dimensions and c) AAO templates comprising uniaxially aligned pores with diameters of 100 nm that imposed complete confinement of the crystals in two dimensions. Fig. 1A displays an SEM image of $MAPbI_3$ deposited on flat SiO_2/Si. On this substrate, $MAPbI_3$ formed crystals on the order of 200 – 800 nm, in agreement with previous reports in the literature.[55] $MAPbI_3$ crystals deposited on nanorod-coated SiO_2 were significantly smaller in comparison, with average diameters of 100 – 500 nm (Fig. 1B). These crystals formed a 500 nm-thick capping layer on top of the nanorods. When deposited in nanoporous AAO templates, the size of $MAPbI_3$ was determined by the pore size (Fig. 1C). In agreement with our previous findings,[54] pore filling in the first 500 nm of the AAO template, in which the average pore diameter is 100 nm, was complete and no capping layer was observed. This depth is commensurate with the active layer thickness of PSCs.[13,56,57] Below the top 500 nm, pore filling was incomplete (Figure S1). For all three samples, as-cast films were yellow in color, which we previously identified to be a PbI_2:DMF complex.[54] Upon thermal annealing, this metastable phase converted to black $MAPbI_3$ crystals.

2D x-ray diffraction (XRD) patterns were collected on the samples before and after storage in air to assess the impact of nanoconfinement on the air stability of $MAPbI_3$ crystals. Before exposure to air, all three samples displayed reflections consistent with $MAPbI_3$ crystals (Fig. 2A, left). The sample deposited in the AAO template also displayed weak reflections associated with the PbI_2:DMF complex, indicating incomplete conversion to the perovskite phase during thermal annealing.

The right column of Fig. 2A displays 2D XRD spectra collected on these samples after extended storage in air with an average humidity of 60% (refer to Figure S2). Over a period of 21 days of exposure to air, the film deposited on SiO_2/Si turned from black to yellow. Diffraction rings associated with $MAPbI_3$ completely disappeared in the 2D XRD pattern collected on the film during this time period. Instead, the (001), (100), (10$\bar{1}$) and (102) reflections of PbI_2 were observed. In contrast, films deposited on AAO nanorods and pores remained black for more than 271 and 594 days, respectively. A weak diffraction ring associated with the (001) reflection of PbI_2 appeared on the 2D XRD pattern collected on the film deposited on AAO nanorods after 271 days of air exposure,

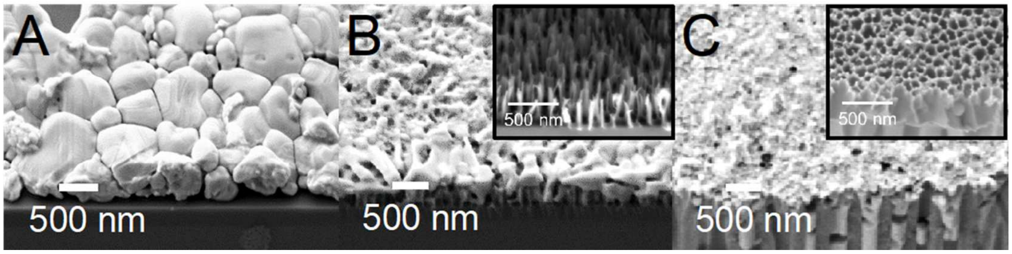

Fig. 1 SEM images of $MAPbI_3$ deposited on A) a SiO_2/Si substrate, B) a SiO_2/Si substrate with AAO NRs and C) a commercial AAO template, respectively. Insets in B and C display an AAO NR-coated substrate and a commercial AAO template, respectively, prior to $MAPbI_3$ deposition.

while no diffraction ring associated with PbI_2 was observed on the 2D XRD pattern collected on the film deposited in AAO pores after 594 days of air exposure.

Fig. 2B displays a graph of the intensities of the (110) reflection of $MAPbI_3$ and the (001) reflection of PbI_2 with respect to air exposure time of the $MAPbI_3$-coated samples. For $MAPbI_3$ deposited on SiO_2/Si, the (110) reflection of $MAPbI_3$ disappeared and the intensity of the (001) reflection of PbI_2 increased significantly after 21 days, indicating the $MAPbI_3$ converted to PbI_2 completely within this period. This observation is in agreement with other reports in the literature on the rapid degradation of $MAPbI_3$ upon exposure to ambient humidity.[58–60]

In contrast, for $MAPbI_3$ crystals deposited on AAO nanorods, the intensity of the (110) reflection of $MAPbI_3$ decreased only 3% over a period of 271 days. In the same time frame, the intensity of the (001) reflection of PbI_2 increased by only 8%, suggesting the stability of $MAPbI_3$ in NRs was significantly improved compared with that on SiO_2/Si. These results support previous findings that PSCs incorporating TiO_2[61,62] and ZnO nanorod[63] scaffolds onto which $MAPbI_3$ was deposited displayed significantly longer lifetimes compared to those incorporating disordered mesoporous TiO_2 scaffolds and planar PSCs. The mechanism for improved stability, however, was unclear. In these samples, the presence of an inert scaffold likely plays a role in suppressing molecular transport. Improved air stability of methylammonium tin iodide nanowires embedded in AAO templates was attributed to suppression of water diffusion into the crystals.[53] Additionally, 9% efficient $MAPbI_3$ PSCs incorporating porous AAO scaffolds were reported to display low hysteresis due to suppressed ion diffusion, which may contribute to long-term air stability.[52]

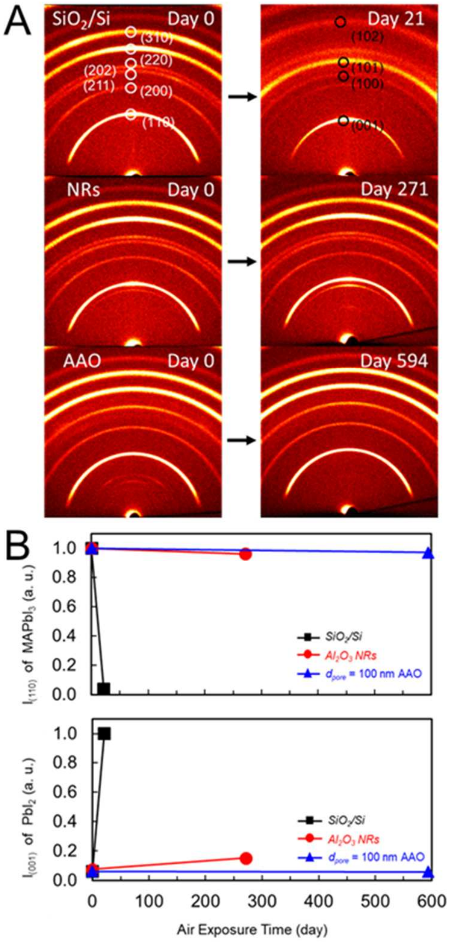

Fig. 2 A) 2D XRD patterns collected on a $MAPbI_3$-coated SiO_2/Si substrate, a SiO_2/Si substrate with AAO nanorods (NRs) and a commercial AAO template infiltrated with $MAPbI_3$ crystals measured at different air exposure time. Major reflections corresponding to $MAPbI_3$ (white) and PbI_2 (black) are labeled. B) Plots of the intensity of the $MAPbI_3$ (110) reflection (top) and the PbI_2 (001) (bottom) versus the length of air exposure time extracted from the 2D XRD patterns.

$MAPbI_3$ crystals deposited in the nanopores of AAO templates displayed the highest stability, with the intensity of the (110) reflection of $MAPbI_3$ remaining constant for a period of 594 days. The diffraction peak associated with PbI_2 was undetectable during this same time period, indicating that $MAPbI_3$ crystals confined within AAO nanopores did not convert to PbI_2 during prolonged exposure to air. Furthermore, the remaining PbI_2:DMF crystal phase present in the AAO templates after thermal annealing disappeared during this time, indicating complete conversion of the precursors to $MAPbI_3$.

Closer examination of the 2D XRD patterns of $MAPbI_3$ films revealed the existence of two distinct polymorphs at RT depending on the structure of the underlying substrate. Typically, the TP is present between temperatures of 162 K and 327 K[64] and forms on both planar[65] and mesoporous substrates[66] in this temperature range. The CP of $MAPbI_3$ is stable at temperatures greater than 327 K and reversibly transitions back to the TP upon cooling. This transition involves a collective rotation of the PbI_2-octahedra around the *c*-axis.[41,67] On flat SiO_2/Si substrates and AAO nanorod-coated substrates, $MAPbI_3$ crystals formed the tetragonal polymorph at RT as expected. This phase was identified by the presence of both the $(211)_T$ and $(202)_T$ reflections at q = 1.65 and q = 1.73 $Å^{-1}$, respectively, in the 2D XRD patterns displayed in Fig. 2. Surprisingly, the diffraction pattern collected at RT on $MAPbI_3$ deposited within AAO nanopores displays a single peak at q = 1.73 $Å^{-1}$, consistent with the $(111)_C$ reflection of the high-temperature CP. Neutron and X-ray diffraction patterns of the CP and TP of $MAPbI_3$ reported by other researchers also display peak splitting upon transitioning from CP to TP.[41]

To investigate the influence of nanoconfinement on the polymorph stability of $MAPbI_3$, temperature-dependent 2D XRD patterns were collected during heating from 293 K to 373 K in 10 K increments. 1D line traces extracted along q_{xy} = 0 $Å^{-1}$ from the 2D XRD patterns are displayed in Fig. 3. As displayed in the figure, both the $(211)_T$ and $(202)_T$ reflections were observed in the diffraction pattern collected on $MAPbI_3$ crystals deposited on SiO_2/Si displayed 323 K. Above this temperature, the peak associated with the $(211)_T$ plane disappeared and merged into a single peak associated with the $(111)_C$ reflection of cubic $MAPbI_3$. For $MAPbI_3$ crystals deposited on AAO nanorods, temperature-dependent XRD patterns revealed that the tetragonal-cubic phase transition occurred between 333 K and 343 K, slightly higher than on SiO_2/Si. These results indicate that the partial confinement of $MAPbI_3$ crystals in the presence of nanorods increases the energy barrier to the solid-state polymorph transition. When deposited in the nanopores of an AAO template,

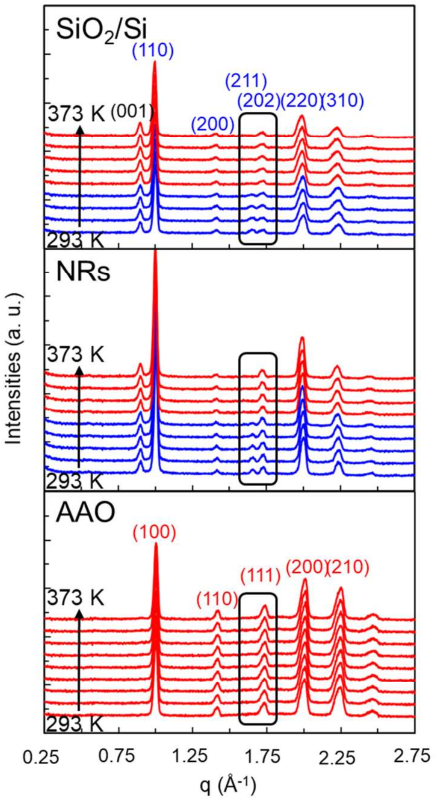

Fig. 3 1D line traces along q_{xy} = 0 Å^{-1} extracted from 2D XRD patterns collected on MAPbI$_3$ crystals deposited on a SiO$_2$/Si substrate (top), an AAO nanorod-coated substrate (middle), and a commercial AAO template (bottom) at temperatures in the range of 293 K to 373 K in increments of 10 K.

MAPbI$_3$ formed the CP even at RT. This phase remained present at all temperatures tested, as displayed in Fig. 3. It is also important to note that the (001) reflection of PbI$_2$ at q = 0.90 Å^{-1} appeared in the diffraction pattern of samples deposited on SiO$_2$ and AAO nanorods, suggesting partial degradation of MAPbI$_3$ into PbI$_2$.

Stabilization of the CP at RT has previously been reported for systems in which MAPbI$_3$ was doped with 20 mol% bromine.[23] Because bromine has a smaller ionic radius compared to iodine, the partial replacement of iodine with bromine ions reduced lattice strain and allowed relaxation of the Pb-I bonds. The presence of chlorine (introduced using precursors PbCl$_2$ or CH$_3$NH$_3$Cl) was similarly found to stabilize the CP at RT.[68] It was suggested that chlorine ions impact the nucleation and growth of MAPbI$_3$ crystals. Recently, the CP phase of formamidinium lead iodide (FAPbI$_3$) was stabilized in nanostructures through the binding of aromatic ammonium cations to the surfaces of the crystals.[69] It was hypothesized that the lowering in surface energy of the nanocrystals stabilized the structures against phase transitions.

Furthermore, room-temperature stabilization of the cubic phase of both MAPbI$_3$[51] and cesium lead iodide[52] nanowires grown by vapor deposition into porous alumina membranes was recently observed. Our findings of CP stabilization in solution-grown, nanoconfined MAPbI$_3$ crystals at RT without chemical modifications, indicate that CP stabilization is independent of deposition procedure and is largely a consequence of confinement. We hypothesize that nanoconfinement introduces strain to the MAPbI$_3$ lattice, thereby hindering phase transformations. Ab initio simulations recently found that uniaxial strain along the [001] direction renders the energy difference between the tetragonal $I4/mcm$ and cubic $Pm\bar{3}m$ phase minimal at RT.[70]

MAPbI$_3$ undergoes a second polymorph transition from TP to OP at around 160 K.[71] According to computational simulations, this phase transition occurs via tilting of PbI$_6$ octahedra and a decrease of the I-H bond length, with H atoms from the MA components. This bond shifting results in a slight volume contraction from 1024.77 to 1006.23 Å^3.[72] Such deformation restricts the rotational degrees of freedom of MA$^+$ cation.[73] Electronically, this phase transition results in an abrupt increase in band gap of around 100 meV,[74–77] which manifests as a shift in photoluminescence (PL) emission.

To further examine the effect of nanoconfinement on the TP-OP phase transition of MAPbI$_3$ crystals, we performed temperature-dependent confocal micro-PL spectroscopy (μPL). The optical

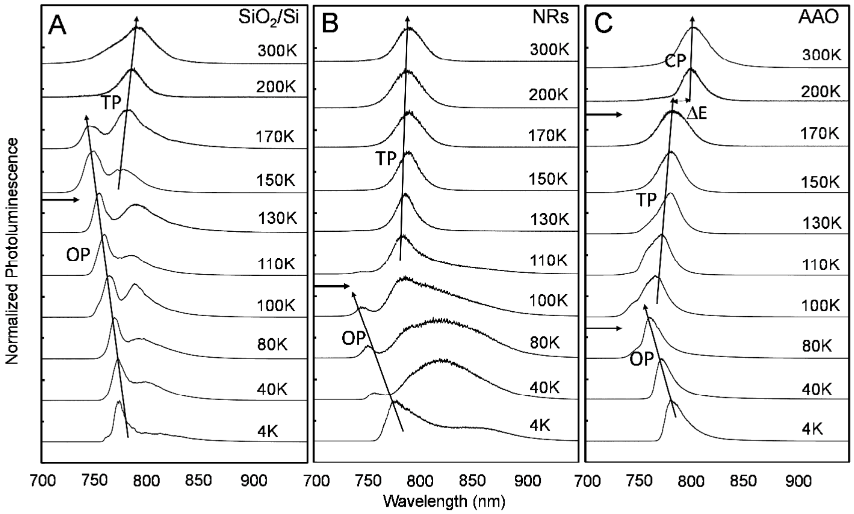

Fig. 4 Normalized temperature-dependent PL spectra of MAPbI$_3$ deposited on a A) SiO$_2$/Si substrate, B) AAO NR-coated SiO$_2$/Si substrate, and C) commercial AAO template measured at temperatures ranging from 4 – 300 K. The arrows denote shifts in the emission peaks, as well as the phase present. Horizontal black arrows near the y axis indicate phase transitions.

response of the $MAPbI_3$ films deposited on substrates with varying extents of nanoconfinement was measured under laser excitation of 533 nm over the temperature range from 4 K to 300 K. Fig. 4A displays the μPL signal for unconfined $MAPbI_3$ deposited on a SiO_2/Si substrate. For clarity, all spectra are normalized to highlight the spectral emission peak shifts. Given that the optical response of $MAPbI_3$ crystals can vary widely depending on the film morphology[78] and direction of temperature ramp (i.e. heating or cooling),[79] the temperature-dependent μPL spectra collected in our study for the case of unconfined $MaPbI_3$ are generally consistent with reports in the literature. As displayed in Fig. 4A, a strong PL peak at 773 nm (1.604 eV), associated with the OP of $MAPbI_3$ was observed at 4 K. This energy position corresponds well with the reported band gap for the OP of $MAPbI_3$, suggesting that emission is dominated by excitons.[80] From 4 K to 170 K, the OP emission peak continuously blue-shifted as a result of reverse ordering of the band edge[32,81–84] until it disappeared above 170 K.

At temperatures below 150 K, a second low-energy peak was also observed. This peak is a common feature of low-temperature $MAPbI_3$ PL spectra[35,55,79,85–87] and has been attributed to either TP inclusions within the OP[31,40,88] or to donor-acceptor pair (DAP) recombination.[55,86,89] Given its presence only at low temperatures and its relatively large linewidth (35 – 43 nm), we attribute this peak to donor-acceptor and other defect-related recombination. Consistent with literature reports, the TP peak was first observed at 150 K and co-existed with the OP up to 170 K. Between 200 – 300 K, only the TP was observed.

In contrast, for $MAPbI_3$ semiconfined within AAO NRs, the evolution of PL spectra from 4 K to 300 K deviated significantly compared to that of unconfined $MAPbI_3$ (Fig. 4B). First of all, the spectra at 40 K and 80 K featured spectrally broad low-energy peaks with linewidths as large as 90 nm. This peak is likely related to the presence of a large distribution of defects in the film acting as recombination centers. Secondly, the high-energy peak associated with OP disappeared already at a temperature of about 110 K, which is significantly lower that the observed 170 – 200 K for the phase transition temperature between OP and TP in unconfined $MAPbI_3$. This suggests that nanoconfinement shifts the thermodynamic equilibrium between the two phases. Size-dependent phase transition temperatures have previously been reported for $MAPbI_3$ microplates, with decreasing phase transition temperature with decreasing platelet thickness.[86] This trend was attributed to surface energy differences between the two polymorphs and increasing surface-to-volume ratio with decreasing platelet thickness.

Fig. 4C displays the temperature-dependent PL spectra for the case of strongly nanoconfined $MAPbI_3$ crystals in AAO templates with 100-nm pores. Unlike the previous two samples, coexistence of a high- and low-energy peak at low temperatures was not observed. The peak at 784 nm in the 4 K spectrum corresponds to the OP emission that quenches above 80 K abruptly. The TP signal dominated the spectra above 80 K and displayed a red-shift from 100 – 170 K. This red-shift in a similar temperature range has been observed by several other groups,[86,88] but not all,[90,91] and its molecular origin remains unclear. In addition, at higher temperatures an abrupt shift in the PL peak location from 783 nm at 170 K to 802 nm at 200 K was observed, corresponding to an energy jump of 32 meV. This jump is consistent with a transition from the TP to the CP, with an expected energy difference of 30 meV according to theoretical calculations.[92] X-ray diffraction experiments confirmed that the CP of $MAPbI_3$ was recovered at 300 K after temperature cycling to 4 K. As a result, under strong nanoconfinement the CP becomes already stable at cryogenic temperatures of 200 K and dominates emission at RT, while the semiconfined and unconfined case do not transform to the CP within the accessible temperature range that is limited to 300 K in these experiments.

Significantly, the absence of a broad, low-energy peak in the low-temperature PL spectra collected on $MAPbI_3$ deposited in AAO nanopores suggests that defects acting as recombination sites are largely absent in these crystals. Indeed, the PL behavior of nanoconfined crystals in Fig. 4C below 100 K corresponds well to that collected previously for the case of unconfined $MAPbI_3$ single crystals that display high quality.[91] In our data, the linewidths of the both the OP and TP peaks ranged from 20 – 35 nm throughout the entire temperature window, significantly lower than that in PL spectra previously reported for $MAPbI_3$.[87,88] Our results suggest that high-quality single $MAPbI_3$ crystals form within individual nanopores in the AAO templates during processing. PL lifetime measurements (Figure S3) confirm that nanoconfined $MAPbI_3$ crystals are of higher quality than unconfined $MAPbI_3$ crystals. Despite an order of magnitude smaller average crystal size, the PL decay time observed in nanoconfined $MAPbI_3$ crystals was measured to be 18.8 ns, 25% longer than that observed for unconfined $MAPbI_3$ crystals deposited on SiO_2/Si. Notably, this PL lifetime is nine times longer than that previously observed for solution-deposited 250-nm diameter $MAPbI_3$ crystals.[93]

Furthermore, we do not observe evidence of coexistence of OP and TP in this case, suggesting that these nanocrystals undergo a rather sharp phase transition. Increased surface-to-volume ratio and surface energy effects at the pore walls likely contribute to the lower observed transition temperature (T = 100 K) compared to the bulk transition temperature of T ~ 170 K between OP and TP. Similar phenomena of melting point depression has been observed in nanoconfined systems.[94] Collectively, these results suggest nanoconfinement to be an effective strategy not only to stabilize $MAPbI_3$ against humidity-induced degradation and temperature-dependent polymorph transitions, but also to improve the quality of the crystals.

The above temperature-dependent PL spectra was collected using a laser spot size of ~850 nm, corresponding to the signal being collected from approximately 40 crystals confined within the 100-nm diameter pores of AAO. To confirm the uniformity of crystal quality in nanoconfined $MAPbI_3$, we performed hyperspectral μPL mapping with an attocube piezo-scanner (see Experimental Section). Specifically, spatially resolved μPL maps were collected at a sample temperature of 100 K on $MAPbI_3$ films deposited on a flat SiO_2/Si substrate and nanoconfined $MAPbI_3$ crystals in an AAO template with 100 nm pores. Fig. 5 displays the μPL maps in which blue (A and D) refers to the integrated intensity filtered around 760 ± 10 nm that covers the OP signal, and red (B and E) refers to the integrated intensity spectrally filtered around 785 ± 10 nm covering the TP signal. Corresponding SEM images at the same magnification are displayed in Fig.s 5C and F. The μPL maps of the $MAPbI_3$ films deposited on the SiO_2/Si substrate (Figs. 5A and B) reveal strong spatial inhomogeneity in the OP and TP emission, consistent with coexistence of the two phases at temperatures below 170 K. Similar observations have been previously reported for $MAPbI_3$.[95,96] In comparison, the μPL maps collected on nanoconfined $MAPbI_3$ (Figs. 5D and E) display a high degree of uniformity in the PL signal throughout the sample, consistent with the temperature-dependent PL spectra indicating the absence of phase coexistence between the TP and OP under nanoconfinement.

Experimental

Perovskite $MAPbI_3$ precursor solution synthesis: $MAPbI_3$ precursor solution was prepared according to a previously reported method.[54] Briefly, an equimolar 35 wt% mixture of PbI_2 (Sigma-Aldrich, 99% purity) and MAI (Dyesol^{TM}) in anhydrous DMF (Sigma-Aldrich) was prepared in a nitrogen environment. The precursor solution was stirred overnight at 70 ^oC.

AAO nanorod synthesis: AAO nanorods grown on SiO_2/Si substrates were fabricated following standard procedures in the literature.[97,98] SiO_2/Si substrates were washed with acetone, methanol and deionized water, and then dried. Samples were then exposed to UV-ozone for 15 minutes. 200 nm of aluminum was thermally deposited onto the cleaned substrates. Anodization of the aluminum film was carried out in the presence of 0.3 M oxalic acid (Sigma-Aldrich, $C_2H_2O_4$, 99%) at 40 V and 13 ^oC to generate AAO. After 1 min, the anodized surfaces were washed with deionized water and dried. Samples were then immersed in 0.1 M aqueous H_3PO_4 for 100 min to partially etch the AAO into nanorod structures.

Preparation of $MAPbI_3$ films on substrates with varying extents of confinement: 50 μl of the precursor solution was drop cast onto flat SiO_2/Si substrates, AAO nanorod-coated SiO_2/Si substrates and nanoporous AAO templates (Whatman$^®$) with nominal pore diameters of 100 nm, respectively. The samples were subsequently spun cast at 2000 rpm for 45 s and were then placed on a hot plate initially at RT. The temperature was increased in 10 ^oC increments every 5 min until a temperature of 95 ^oC was reached. The samples were then transferred to another hot plate at 130 ^oC for 5 min.

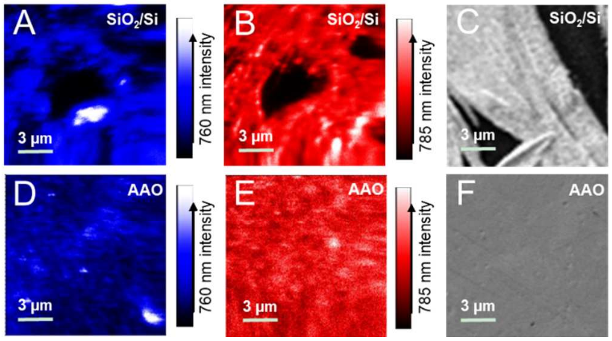

Fig. 5 Spatially resolved μPL maps at collected at 100 K for A) $MAPbI_3$ deposited on SiO_2/Si at λ = 760 nm, B) the same spot at λ = 785 nm, D) $MAPbI_3$ deposited in the nanopores of commercial AAO templates at λ = 760 nm, and E) the same spot at λ = 785 nm. C and F) Top-view SEM images of $MAPbI_3$ deposited on a SiO_2/Si substrate and a commercial AAO template, respectively.

2D x-ray diffraction measurements: 2D x-ray diffraction patterns (XRD) were collected on the samples using a Bruker AXS D8 DISCOVER GADDS diffractometer with VANTEC 2000 detector. The diffractometer was operated in reflection mode at 40 kV and 40 mA. Data was collected using an incident x-ray wavelength of λ = 1.5405 Å and at an incident angle of 3^o. XRD patterns were collected in air at RT for 120 s. Samples were initially stored in an N_2-filled container to prevent air exposure prior to data collection, and subsequently stored in ambient air for stability studies.

Temperature-dependent XRD measurements: Samples were placed on a hot stage installed in the diffractometer mentioned above. The temperature was increased from RT at a speed of 10 K/min. 2D XRD patterns were collected on the samples at temperatures ranging from 293 – 383 K in 10 K increments.

Photoluminescence spectroscopy: Samples were placed in a closed-cycle cryogen-free cryostat with the accessible temperature range 4 – 300 K and ultralow vibration (attodry1100 from attocube) at a pressure of 10^{-6} bar. A green laser diode, emitting at 533 nm in continuous wave mode at a power of 7 μW, was used for excitation. A diffraction-limited laser spot size of ~ 0.85 microns was achieved using a cryogenic microscope objective with numerical aperture of 0.82. The relative position between sample and laser spot was adjusted with a piezo-electric xyz-stepper while 2D scan images were recorded with a 2D-piezo scanner (attocube). The μPL emission from the sample was collected in a single mode fiber and dispersed using a 0.75 m focal length spectrometer equipped with a liquid nitrogen cooled silicon CCD camera. To realize hyperspectral images the signal was sent through optical band pass filters, as further detailed in Ref. 99.

Conclusions

We have examined the impact of nanoconfinement on $MAPbI_3$ stability against humidity and temperature-dependent polymorph transitions. While $MAPbI_3$ deposited on an SiO_2/Si substrate degraded to PbI_2 completely after only 21 days of exposure to ambient air, $MAPbI_3$ crystals nanoconfined in AAO nanorod-coated SiO_2 and nanoporous AAO templates remained stable for an unprecedented 271 and 594 days, respectively, without any need to passivation or encapsulation. 2D XRD patterns of $MAPbI_3$ films revealed that both partial and complete 2D nanoconfinement further affect temperature-dependent polymorph stability. Most notably, μPL spectra revealed that the high-temperature cubic phase of $MAPbI_3$ that typically forms above 330 K was stabilized to temperatures as low as 170 K when $MAPbI_3$ was nanoconfined in AAO nanopores. Such stability is an important consideration in the operation of solar cells, where small changes to the crystal structure can manifest as large changes in device performance. Spatially-resolved μPL maps further revealed that nanoconfinement produces high-quality $MAPbI_3$ nanocrystals exhibiting spatial uniformity. Collectively, the present findings demonstrate nanoconfinement as a viable strategy for stabilizing $MAPbI_3$ crystals and reveal novel insights about phase transformation in these systems.

Conflicts of interest

There are no conflicts to declare.

Acknowledgements

The authors are grateful for the assistance of Dr. Chunhua Hu at the Department of Chemistry of New York University with 2D XRD experiments, and C.H. acknowledges support by the National Science Foundation under Award Numbers CRIF/CHE-0840277 and by the NSF MRSEC Program under Award Number DMR-0820341. S.S. and S.S.L. acknowledge financial support under NSF award ECCS-MRI-1531237. Research used microscopy resources within the Laboratory for Multiscale Imaging at Stevens Institute of Technology and the authors thank Dr. Tsengming Chou for assistance.

References

1 Average monthly humidity in Hoboken, United States of America, https://weather-and-climate.com/average-monthly-Humidity-perc,hoboken-new-jersey-us,United-States-of-America, (accessed 29 March 2018).
2 M. A. Green, A. Ho-Baillie and H. J. Snaith, *Nat Phot.*, 2014, **8**, 506–514.
3 Y.-C. Hsiao, T. Wu, M. Li, Q. Liu, W. Qin and B. Hu, *J. Mater. Chem. A*, 2015, **3**, 15372–15385.
4 M. Liu, M. B. Johnston and H. J. Snaith, *Nature*, 2013, **501**, 395–398.
5 M. A. Green, K. Emery, Y. Hishikawa, W. Warta and E. D. Dunlop, *Prog. Photovoltaics Res. Appl.*, 2015, **23**, 805–812.
6 J. Seo, J. H. Noh and S. Il Seok, *Acc. Chem. Res.*, 2016, **49**, 562–572.
7 M. M. Lee, *Science*, 2012, **338**, 643–647.
8 Y. Zhou, C. Fuentes-Hernandez, J. Shim, J. Meyer, A. J. Giordano, H. Li, P. Winget, T. Papadopoulos, H. Cheun, J. Kim, M. Fenoll, A. Dindar, W. Haske, E. Najafabadi, T. M. Khan, H. Sojoudi, S. Barlow, S. Graham, J.-L. Bredas, S. R. Marder, A. Kahn and B. Kippelen, *Science*, 2012, **336**, 327–332.
9 W. Chen, Y. Wu, Y. Yue, J. Liu, W. Zhang, X. Yang, H. Chen, E. Bi, I. Ashraful, M. Grätzel and L. Han, *Science*, 2015, **350**, 944–948.
10 W. S. Yang, J. H. Noh, N. J. Jeon, Y. C. Kim, S. Ryu, J. Seo and S. Il Seok, *Science*, 2015, **348**, 1234–7.
11 J. Zhao, Y. Li, G. Yang, K. Jiang, H. Lin, H. Ade, W. Ma and H. Yan, *Nat. Energy*, 2016, **1**, 15027.
12 T. Baikie, Y. Fang, J. M. Kadro, M. Schreyer, F. Wei, S. G. Mhaisalkar, M. Graetzel, T. J. White, M. G. Kanatzidis, J. E. Moser, M. Grätzel and N. G. Park, *J. Mater. Chem. A*, 2013, **1**, 5628.
13 C. S. Ponseca, T. J. Savenije, M. Abdellah, K. Zheng, A. Yartsev, T. Pascher, T. Harlang, P. Chabera, T. Pullerits, A. Stepanov, J. P. Wolf and V. Sundström, *J. Am. Chem. Soc.*, 2014, **136**, 5189–5192.
14 H. Oga, A. Saeki, Y. Ogomi, S. Hayase and S. Seki, *J. Am. Chem. Soc.*, 2014, **136**, 13818–13825.
15 D. B. Mitzi, *J. Chem. Soc. Dalt. Trans.*, 2001, **0**, 1–12.
16 C. C. Stoumpos, C. D. Malliakas and M. G. Kanatzidis, *Inorg. Chem.*, 2013, **52**, 9019–9038.
17 C. M. Proctor, M. Kuik and T.-Q. Nguyen, *Prog. Polym. Sci.*, 2013, **38**, 1941–1960.
18 G. Xing, N. Mathews, S. Sun, S. S. Lim, Y. M. Lam, M. Grätzel, S. Mhaisalkar and T. C. Sum, *Science*, 2013, **342**, 344–7.
19 S. D. Stranks, G. E. Eperon, G. Grancini, C. Menelaou, M. J. P. Alcocer, T. Leijtens, L. M. Herz, A. Petrozza and H. J. Snaith, *Science*, 2013, **342**, 341–344.
20 Y. Rong, L. Liu, A. Mei, X. Li and H. Han, *Adv. Energy Mater.*, 2015, **5**, 1501066.
21 T. Leijtens, G. E. Eperon, N. K. Noel, S. N. Habisreutinger, A. Petrozza and H. J. Snaith, *Adv. Energy Mater.*, 2015, **5**, 1500963.
22 G. Niu, X. Guo and L. Wang, *J. Mater. Chem. A*, 2015, **3**, 8970–8980.
23 J. H. Noh, S. H. Im, J. H. Heo, T. N. Mandal and S. Il Seok, *Nano Lett.*, 2013, **13**, 1764–1769.
24 Y. Zhou, C. Fuentes-Hernandez, J. Shim, J. Meyer, A. J. Giordano, H. Li, P. Winget, T. Papadopoulos, H. Cheun, J. Kim, M. Fenoll, A. Dindar, W. Haske, E. Najafabadi, T. M. Khan, H. Sojoudi, S. Barlow, S. Graham, J. L. Brédas, S. R. Marder, A. Kahn and B. Kippelen, *Science (80-.).*, 2012, **336**, 327–332.
25 W. Ke, C. Xiao, C. Wang, B. Saparov, H.-S. Duan, D. Zhao, Z. Xiao, P. Schulz, S. P. Harvey, W. Liao, W. Meng, Y. Yu, A. J. Cimaroli, C.-S. Jiang, K. Zhu, M. Al-Jassim, G. Fang, D. B. Mitzi and Y. Yan, *Adv. Mater.*, 2016, **28**, 5214–5221.
26 N. Ahn, D.-Y. Son, I.-H. Jang, S. M. Kang, M. Choi and N.-G. Park, *J. Am. Chem. Soc.*, 2015, **137**, 8696–8699.
27 Y. Han, S. Meyer, Y. Dkhissi, K. Weber, J. M. Pringle, U. Bach, L. Spiccia and Y.-B. Cheng, *J. Mater. Chem. A*, 2015, **3**, 8139–8147.
28 N. Tripathi, M. Yanagida, Y. Shirai, T. Masuda, L. Han and K. Miyano, *J. Mater. Chem. A*, 2015, **3**, 12081–12088.
29 G. Abdelmageed, L. Jewell, K. Hellier, L. Seymour, B. Luo, F. Bridges, J. Z. Zhang and S. Carter, *Appl. Phys. Lett.*, 2016, **109**, 233905.
30 T. Baikie, Y. Fang, J. M. Kadro, M. Schreyer, F. Wei, S. G. Mhaisalkar, M. Graetzel and T. J. White, *J. Mater. Chem. A*, 2013, **1**, 5628.
31 C. Wehrenfennig, M. Liu, H. J. Snaith, M. B. Johnston and L. M. Herz, *APL Mater.*, 2014, **2**, 81513.
32 V. D'Innocenzo, G. Grancini, M. J. P. Alcocer, A. R. S. Kandada, S. D. Stranks, M. M. Lee, G. Lanzani, H. J. Snaith and A. Petrozza, *Nat. Commun.*, 2014, **5**, 3586.
33 K. Galkowski, A. Mitioglu, A. Miyata, P. Plochocka, O. Portugall, G. E. Eperon, J. T.-W. Wang, T. Stergiopoulos, S. D. Stranks, H. J. Snaith and R. J. Nicholas, *Energy Environ. Sci.*, 2016, **9**, 962–970.

34 D. Li, G. Wang, H. C. Cheng, C. Y. Chen, H. Wu, Y. Liu, Y. Huang and X. Duan, *Nat. Commun.*, 2016, **7**, 11330.
35 R. L. Milot, G. E. Eperon, H. J. Snaith, M. B. Johnston and L. M. Herz, *Adv. Funct. Mater.*, 2015, **25**, 6218–6227.
36 C. Quarti, E. Mosconi, J. M. Ball, V. D'Innocenzo, C. Tao, S. Pathak, H. J. Snaith, A. Petrozza and F. De Angelis, *Energy Environ. Sci.*, 2016, **9**, 155–163.
37 N. Onoda-Yamamuro, T. Matsuo and H. Suga, *J. Phys. Chem. Solids*, 1990, **51**, 1383–1395.
38 N. Onoda-Yamamuro, T. Matsuo and H. Suga, *J. Phys. Chem. Solids*, 1992, **53**, 935–939.
39 H. Zhang, X. Qiao, Y. Shen, T. Moehl, S. M. Zakeeruddin, M. Grätzel and M. Wang, *J. Mater. Chem. A*, 2015, **3**, 11762–11767.
40 C. Wehrenfennig, M. Liu, H. J. Snaith, M. B. Johnston and L. M. Herz, *APL Mater.*, 2014, **2**, 81513.
41 P. S. Whitfield, N. Herron, W. E. Guise, K. Page, Y. Q. Cheng, I. Milas and M. K. Crawford, *Sci. Rep.*, 2016, **6**, 35685.
42 I. Borriello, G. Cantele and D. Ninno, *Phys. Rev. B*, 2008, **77**, 235214.
43 T. Baikie, Y. Fang, J. M. Kadro, M. Schreyer, F. Wei, S. G. Mhaisalkar, M. Graetzel and T. J. White, *J. Mater. Chem. A*, 2013, **1**, 5628.
44 Q. Jiang, C. Hu and M. D. Ward, *J. Am. Chem. Soc.*, 2013, **135**, 2144–2147.
45 J. M. Ha, B. D. Hamilton, M. A. Hillmyer and M. D. Ward, *Cryst. Growth Des.*, 2009, **9**, 4766–4777.
46 M. Beiner, G. T. Rengarajan, S. Pankaj, D. Enke and M. Steinhart, *Nano Lett.*, 2007, **7**, 1381–1385.
47 G. T. Rengarajan, D. Enke and M. Beiner, *Open Phys. Chem. J.*, 2007, **1**, 18–24.
48 G. T. Rengarajan, D. Enke, M. Steinhart and M. Beiner, *Phys. Chem. Chem. Phys.*, 2011, **13**, 21367.
49 J. M. Ha, J. H. Wolf, M. A. Hillmyer and M. D. Ward, *J. Am. Chem. Soc.*, 2004, **126**, 3382–3383.
50 H. C. Kwon, A. Kim, H. Lee, D. Lee, S. Jeong and J. Moon, *Adv. Energy Mater.*, 2016, **6**, 1601055.
51 L. Gu, M. M. Tavakoli, D. Zhang, Q. Zhang, A. Waleed, Y. Xiao, K. H. Tsui, Y. Lin, L. Liao, J. Wang and Z. Fan, *Adv. Mater.*, 2016, **28**, 9713–9721.
52 A. Waleed, M. M. Tavakoli, L. Gu, S. Hussain, D. Zhang, S. Poddar, Z. Wang, R. Zhang and Z. Fan, *Nano Lett.*, 2017, **17**, 4951–4957.
53 A. Waleed, M. M. Tavakoli, L. Gu, Z. Wang, D. Zhang, A. Manikandan, Q. Zhang, R. Zhang, Y.-L. Chueh and Z. Fan, *Nano Lett.*, 2017, **17**, 523–530.
54 S. Lee, J. Feldman and S. S. Lee, *Cryst. Growth Des.*, 2016, **16**, 4744–4751.
55 W. Kong, Z. Ye, Z. Qi, B. Zhang, M. Wang, A. Rahimi-Iman and H. Wu, *Phys. Chem. Chem. Phys.*, 2015, **17**, 16405–16411.
56 D. Liu and T. L. Kelly, *Nat. Photonics*, 2014, **8**, 133–138.
57 W. S. Yang, J. H. Noh, N. J. Jeon, Y. C. Kim, S. Ryu, J. Seo and S. Il Seok, *Science (80-.).*, 2015, **348**, 1234–1237.
58 G. E. Eperon, V. M. Burlakov, P. Docampo, A. Goriely and H. J. Snaith, *Adv. Funct. Mater.*, 2014, **24**, 151–157.
59 J. H. Noh, S. H. Im, J. H. Heo, T. N. Mandal and S. Il Seok, *Nano Lett.*, 2013, **13**, 1764–1769.
60 G. Niu, W. Li, F. Meng, L. Wang, H. Dong and Y. Qiu, *J. Mater. Chem. A*, 2014, **2**, 705–710.
61 A. Fakharuddin, F. Di Giacomo, I. Ahmed, Q. Wali, T. M. Brown and R. Jose, *J. Power Sources*, 2015, **283**, 61–67.
62 A. Fakharuddin, F. Di Giacomo, A. L. Palma, F. Matteocci, I. Ahmed, S. Razza, A. D'Epifanio, S. Licoccia, J. Ismail, A. Di Carlo, T. M. Brown and R. Jose, *ACS Nano*, 2015, **9**, 8420–8429.
63 D. Bi, G. Boschloo, S. Schwarzmüller, L. Yang, E. M. J. Johansson and A. Hagfeldt, *Nanoscale*, 2013, **5**, 11686–91.
64 Claudio Quarti, Edoardo Mosconi, J. M. Ball, Valerio D'Innocenzo, Chen Tao, Sandeep Pathak, H. J. Snaith, Annamaria Petrozza and F. D. Angelis, *Energy Environ. Sci.*, 2016, **9**, 155–163.
65 F. Huang, Y. Dkhissi, W. Huang, M. Xiao, I. Benesperi, S. Rubanov, Y. Zhu, X. Lin, L. Jiang, Y. Zhou, A. Gray-Weale, J. Etheridge, C. R. McNeill, R. A. Caruso, U. Bach, L. Spiccia and Y. B. Cheng, *Nano Energy*, 2014, **10**, 10–18.
66 J. Burschka, N. Pellet, S. J. Moon, R. Humphry-Baker, P. Gao, M. K. Nazeeruddin and M. Grätzel, *Nature*, 2013, **499**, 316–319.
67 Y. Kawamura, H. Mashiyama and K. Hasebe, *J. Phys. Soc. Japan*, 2002, **71**, 1694–1697.
68 Q. Wang, M. Lyu, M. Zhang, J. H. Yun, H. Chen and L. Wang, *J. Phys. Chem. Lett.*, 2015, **6**, 4379–4384.
69 Y. Fu, T. Wu, J. Wang, J. Zhai, M. J. Shearer, Y. Zhao, R. J. Hamers, E. Kan, K. Deng, X. Y. Zhu and S. Jin, *Nano Lett.*, 2017, **17**, 4405–4414.
70 K. P. Ong, T. W. Goh, Q. Xu and A. Huan, *J. Phys. Chem. A*, 2015, **119**, 11033–11038.
71 K. Galkowski, A. A. Mitioglu, A. Surrente, Z. Yang, D. K. Maude, P. Kossacki, G. E. Eperon, J. T.-W. Wang, H. J. Snaith, P. Plochocka and R. J. Nicholas, *Nanoscale*, 2017, **9**, 3222–3230.
72 K. P. Ong, T. W. Goh, Q. Xu and A. Huan, *J. Phys. Chem. Lett.*, 2015, **6**, 681–685.
73 C. Motta, F. El-Mellouhi, S. Kais, N. Tabet, F. Alharbi and S. Sanvito, *Nat. Commun.*, 2015, **6**, 7026.
74 T. Baikie, Y. Fang, J. M. Kadro, M. Schreyer, F. Wei, S. G. Mhaisalkar, M. Graetzel and T. J. White, *J. Mater. Chem. A*, 2013, **1**, 5628.
75 V. D'Innocenzo, G. Grancini, M. J. P. Alcocer, A. R. S. Kandada, S. D. Stranks, M. M. Lee, G. Lanzani, H. J. Snaith and A. Petrozza, *Nat. Commun.*, 2014, **5**, 3586.
76 J. Even, L. Pedesseau and C. Katan, *J. Phys. Chem. C*, 2014, **118**, 11566–11572.
77 Y. Yamada, Y., Nakamura, T., Endo, M., Wakamiya, A. & Kanemitsu, *Photovoltaics*, 2015, **5**, 401–405.
78 D. Li, G. Wang, H. C. Cheng, C. Y. Chen, H. Wu, Y. Liu, Y. Huang and X. Duan, *Nat. Commun.*, 2016, **7**, 11330.
79 A. Osherov, E. M. Hutter, K. Galkowski, R. Brenes, D. K. Maude, R. J. Nicholas, P. Plochocka, V. Bulović, T. J. Savenije and S. D. Stranks, *Adv. Mater.*, 2016, **28**, 10757–10763.
80 A. Amat, E. Mosconi, E. Ronca, C. Quarti, P. Umari, M. K. Nazeeruddin, M. Grätzel and F. De Angelis, *Nano Lett.*,

2014, **14**, 3608–3616.
81 R. L. Milot, G. E. Eperon, H. J. Snaith, M. B. Johnston and L. M. Herz, *Adv. Funct. Mater.*, 2015, **25**, 6218–6227.
82 M. A. Green, A. Ho-Baillie and H. J. Snaith, *Nat. Photonics*, 2014, **8**, 506–514.
83 J. Even, L. Pedesseau, C. Katan, M. Kepenekian, J.-S. Lauret, D. Sapori and E. Deleporte, *J. Phys. Chem. C*, 2015, **119**, 10161–10177.
84 T. Ishihara, *J. Lumin.*, 1994, **60**–**61**, 269–274.
85 C. Wehrenfennig, M. Liu, H. J. Snaith, M. B. Johnston and L. M. Herz, *Energy Environ. Sci.*, 2014, **7**, 2269–2275.
86 H.-H. Fang, R. Raissa, M. Abdu-Aguye, S. Adjokatse, G. R. Blake, J. Even and M. A. Loi, *Adv. Funct. Mater.*, 2015, **25**, 2378–2385.
87 A. D. Wright, C. Verdi, R. L. Milot, G. E. Eperon, M. A. Pérez-Osorio, H. J. Snaith, F. Giustino, M. B. Johnston and L. M. Herz, *Nat. Commun.*, 2016, **7**, 11755.
88 K. Wu, A. Bera, C. Ma, Y. Du, Y. Yang, L. Li and T. Wu, *Phys. Chem. Chem. Phys.*, 2014, **16**, 22476–22481.
89 G. Xing, N. Mathews, S. S. Lim, N. Yantara, X. Liu, D. Sabba, M. Grätzel, S. Mhaisalkar and T. C. Sum, *Nat. Mater.*, 2014, **13**, 476–480.
90 R. L. Milot, G. E. Eperon, H. J. Snaith, M. B. Johnston and L. M. Herz, *Adv. Funct. Mater.*, 2015, **25**, 6218–6227.
91 H. H. Fang, R. Raissa, M. Abdu-Aguye, S. Adjokatse, G. R. Blake, J. Even and M. A. Loi, *Adv. Funct. Mater.*, 2015, **25**, 2378–2385.
92 S. X. Tao, X. Cao and P. A. Bobbert, *Sci. Rep.*, 2017, **7**, 14386.
93 V. D’Innocenzo, A. R. Srimath Kandada, M. De Bastiani, M. Gandini and A. Petrozza, *J. Am. Chem. Soc.*, 2014, **136**, 17730–17733.
94 Q. Jiang and M. D. Ward, *Chem. Soc. Rev.*, 2014, **43**, 2066–2079.
95 K. Galkowski, A. Mitioglu, A. Surrente, Z. Yang, D. K. Maude, P. Kossacki, G. E. Eperon, J. T.-W. Wang, H. J. Snaith, P. Plochocka and R. J. Nicholas, *Nanoscale*, 2016, **9**, 3222–3230.
96 G. Li, Z. K. Tan, D. Di, M. L. Lai, L. Jiang, J. H. W. Lim, R. H. Friend and N. C. Greenham, *Nano Lett.*, 2015, **15**, 2640–2644.
97 L. Luo, C.-J. Lin, C.-Y. Tsai, H.-P. Wu, L.-L. Li, C.-F. Lo, C.-Y. Lin and E. W.-G. Diau, *Phys. Chem. Chem. Phys.*, 2010, **12**, 1064–1071.
98 M. J. Ashley, M. N. O’Brien, K. R. Hedderick, J. A. Mason, M. B. Ross and C. A. Mirkin, *J. Am. Chem. Soc.*, 2016, **138**, 10096–10099.
99 Y. Luo, E. D. Ahmadi, K. Shayan, Y. Ma, K. S. Mistry, C. Zhang, J. Hone, J. L. Blackburn and S. Strauf, *Nat. Commun.*, 2017, **8**, 1413.

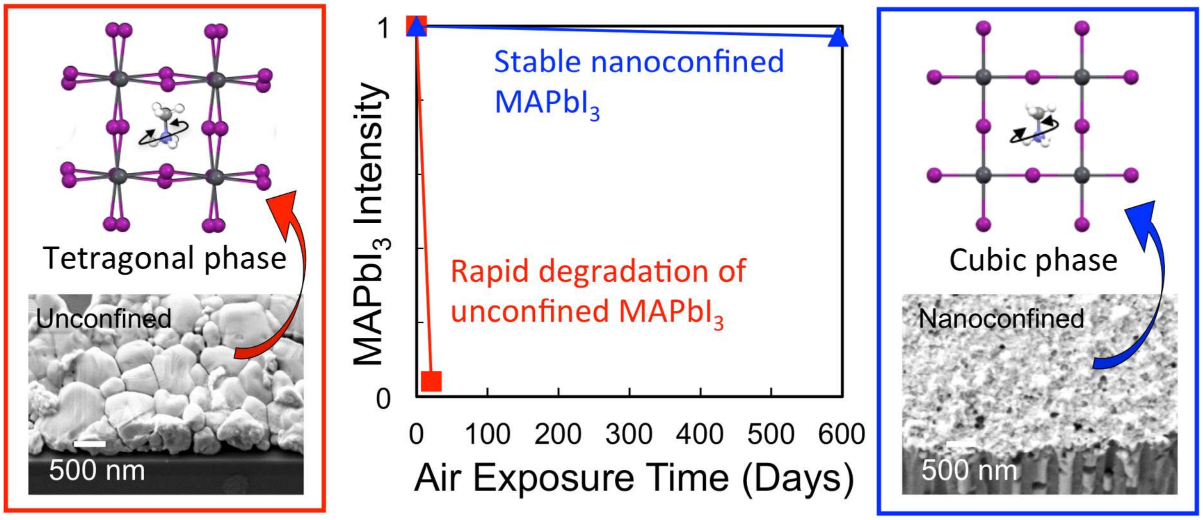

MAPbI$_3$ stability is dramatically improved under nanoconfinement, accompanied by a suppression of polymorph transitions that are detrimental to optoelectronic performance.